

# Dark Energy Constraints from the Thermal Sunyaev Zeldovich Power Spectrum

Boris Bolliet,<sup>1,4</sup> Barbara Comis,<sup>1</sup> Eiichiro Komatsu,<sup>2,3</sup> Juan Francisco Macías-Pérez<sup>1</sup>

<sup>1</sup>*Laboratoire de Physique Subatomique et de Cosmologie, Université Grenoble-Alpes, CNRS/IN2P3, 53, avenue des Martyrs, 38026 Grenoble cedex, France*

<sup>2</sup>*Max-Planck-Institut für Astrophysik, Karl-Schwarzschild Strasse 1, 85748 Garching, Germany*

<sup>3</sup>*Kavli Institute for the Physics and Mathematics of the Universe (Kavli IPMU, WPI), Todai Institutes for Advanced Study, University of Tokyo, Kashiwa 277-8583, Japan*

<sup>4</sup>*Jodrell Bank Centre for Astrophysics, School of Physics and Astronomy, The University of Manchester, Manchester, M13 9PL, U.K.*

28 March 2018

## ABSTRACT

We constrain the dark energy equation of state parameter,  $w$ , using the power spectrum of the thermal Sunyaev-Zeldovich (tSZ) effect. We improve upon previous analyses by taking into account the trispectrum in the covariance matrix and marginalising over the foreground parameters, the correlated noise, the mass bias  $B$  in the Planck universal pressure profile, and all the relevant cosmological parameters (i.e., not just  $\Omega_m$  and  $\sigma_8$ ). We find that the amplitude of the tSZ power spectrum at  $\ell \lesssim 10^3$  depends primarily on  $F \equiv \sigma_8(\Omega_m/B)^{0.40}h^{-0.21}$ , where  $B$  is related to more commonly used variable  $b$  by  $B = (1 - b)^{-1}$ . We measure this parameter with 2.6% precision,  $F = 0.460 \pm 0.012$  (68% CL). By fixing the bias to  $B = 1.25$  and adding the local determination of the Hubble constant  $H_0$  and the amplitude of the primordial power spectrum constrained by the Planck Cosmic Microwave Background (CMB) data, we find  $w = -1.10 \pm 0.12$ ,  $\sigma_8 = 0.802 \pm 0.037$ , and  $\Omega_m = 0.265 \pm 0.022$  (68% CL). Our limit on  $w$  is consistent with and is as tight as that from the distance-alone constraint from the CMB and  $H_0$ . Finally, by combining the tSZ power spectrum and the CMB data we find, in the  $\Lambda$  Cold Dark Matter (CDM) model, the mass bias of  $B = 1.71 \pm 0.17$ , i.e.,  $1 - b = 0.58 \pm 0.06$  (68% CL).

**Key words:** Cosmology: cosmic microwave background – theory – observations – cosmological parameters – dark energy; Galaxies: clusters.

## 1 INTRODUCTION

Clusters of galaxies are the largest gravitationally bound objects in the universe and constitute compelling probes for cosmological studies. In particular, the angular power spectrum of the thermal Sunyaev Zeldovich (tSZ) effect (Sunyaev & Zeldovich 1972) depends sensitively on the amplitude of matter fluctuations (Komatsu & Kitayama 1999; Komatsu & Seljak 2002). While at large multipoles ( $\ell \gtrsim 10^3$ ) the power spectrum depends also on the details of pressure profiles within halos, at smaller multipoles the dependence is much weaker (Komatsu & Kitayama 1999; McCarthy et al. 2014). This makes the tSZ power spectrum at  $\ell \lesssim 10^3$  a powerful probe of cosmology.

Dark energy slows down structure formation (see Weinberg et al. 2013, for a recent review). A less negative value of the dark energy equation of state (EoS) parameter,  $w$ , makes dark energy dominate at higher redshifts, suppressing the growth of structure, hence the present-day matter amplitude parameter  $\sigma_8$ . Using this anti-correlation between  $w$

and  $\sigma_8$  (Komatsu et al. 2009), we can constrain the nature of dark energy. We achieve this by comparing the amplitude of matter fluctuations in a late time universe with that at the last scattering surface of the cosmic microwave background (CMB).

The Planck Collaboration delivered an all-sky map of the Compton  $y$  parameter as well as an estimate of the angular power spectrum up to  $\ell \simeq 1300$  (Planck Collaboration 2013b, 2015). They obtained a constraint on the parameter combination  $\sigma_8\Omega_m^{3/8}$ , with the nuisance parameters such as the foreground contaminants and residual correlated noise marginalised over, but with the mass bias and all the other cosmological parameters fixed, and with the power spectrum covariance matrix containing only a Gaussian term. Horowitz & Seljak (2017) revisited the Planck analysis by including the trispectrum term in the covariance, but held the nuisance parameters fixed at the best-fitting values obtained by the Planck Collaboration. Hurier & Lacasa (2017) varied the mass bias, included the trispectrum in the covari-

	$A_0$	$a_0$	$b_0$	$c_0$	$A_z$	$a_z$	$b_z$	$c_z$		
Bocquet et al. (2016)	0.228	2.15	1.69	1.30	0.285	-0.058	-0.366	-0.045		
Tinker et al. (2008)	0.186	1.47	2.57	1.19	-0.14	-0.06	-0.011	0		
	$\alpha_0$	$\beta_0$	$\gamma_0$	$\eta_0$	$\phi_0$	$\alpha_z$	$\beta_z$	$\gamma_z$	$\eta_z$	$\phi_z$
Tinker et al. (2010)	0.368	0.589	0.864	-0.243	-0.729	0	0.2	-0.01	0.27	-0.08

**Table 1.** Parameters for the halo mass functions (HMF). Note that these parameters values are relevant for Bocquet et al. (2016), Tinker et al. (2008) and Tinker et al. (2010) HMFs evaluated at the over-density mass  $M_{200m}$  (for the Tinker et al. (2008) formula at  $M_{1600m}$ , the value of  $b_z$  has to be replaced by  $b_z = -0.314$ ). Given a parameter  $p = A, b, \dots$ , the redshift dependence is obtained as  $p = p_0(1+z)^{P_z}$ .

ance but used a different method for the tSZ power spectrum estimation. Salvati et al. (2017) included the trispectrum and varied the mass bias and all the relevant cosmological parameters, but not the amplitude of the foreground contaminants and correlated noise.

In this paper, we obtain constraints on the parameter combination that determines the amplitude of the tSZ power spectrum at  $\ell \lesssim 10^3$  and  $w$  by including the trispectrum in the covariance, as well as by varying the mass bias, the nuisance parameters, and all the relevant cosmological parameters.

The rest of the paper is organized as follows. In section 2 we describe main steps of our calculation of the tSZ power spectrum and its numerical implementation. In section 3 we find the parameter combination that scales the amplitude of the tSZ power. In section 4 we present settings of our likelihood analysis and show importance of the non-Gaussian contribution to the covariance matrix. In section 5 we present our cosmological constraints. We conclude in section 6.

## 2 MODEL FOR THE TSZ POWER SPECTRUM

Our model consists of the halo mass function (HMF) and the pressure profile of the intra-cluster medium (ICM). We consider only the 1-halo contribution, as the 2-halo term contribution to the tSZ power spectrum is not significant compared to precision of the current data (Komatsu & Kitayama 1999).

For numerical calculations of the tSZ power spectrum (and trispectrum), we have developed a version of the publicly-available package `class` (Lesgourgues 2011; Blas et al. 2011) augmented with a tSZ module in C. The code is dubbed `class_sz` and is available on the internet<sup>1</sup>. Our code builds upon and improves performance of the previous code `szfast` in Fortran 90 (Komatsu & Seljak 2002; Dolag et al. 2016).

The tSZ angular power spectrum is calculated via

$$C_\ell^{\text{tSZ}} = \int_{z_{\min}}^{z_{\max}} dz \frac{dV}{dz d\Omega} \int_{\ln M_{\min}}^{\ln M_{\max}} d \ln M \frac{dn}{d \ln M} |y_\ell(M, z)|^2, \quad (1)$$

where  $y_\ell$  is the two dimensional Fourier transform of an electron pressure profile,  $dn/dM$  is the HMF, and  $M$  is a characteristic mass of dark matter halos which will be defined more precisely later. The integration over mass is performed using a Gaussian quadrature method within the mass range of

$M_{\min} = 10^{11} h^{-1} M_\odot$  and  $M_{\max} = 5 \times 10^{15} h^{-1} M_\odot$ , where  $h \equiv H_0/100$  is the reduced Hubble constant and  $M_\odot$  is the solar mass. This mass range is chosen so that the integral over the mass converges. In Eq. (1),  $V$  is the comoving volume of the universe and its derivative with respect to redshift  $z$  and solid angle  $\Omega$  is given by

$$\frac{dV}{dz d\Omega} = (1+z)^2 d_A^2(z) c/H(z), \quad (2)$$

where  $c$  is the speed of light,  $d_A(z)$  is the physical angular diameter distance, and  $H(z)$  the Hubble expansion rate.

The integration over redshift is carried out with a simple trapezoidal rule from  $z_{\min} = 0$  and up to  $z_{\max} = 6$ . At higher redshift the number density of halos is vanishingly small.

Using Limber's approximation, the two dimensional Fourier transform of an electron pressure profile  $P_e$  is given by (see, e.g., Komatsu & Seljak 2002)

$$y_\ell = \frac{\sigma_T}{m_e c^2} \frac{4\pi r_{500}}{\ell_{500}^2} \int_{x_{\min}}^{x_{\max}} dx x^2 \frac{\sin(\ell x/\ell_{500})}{\ell x/\ell_{500}} P_e(x), \quad (3)$$

where  $\sigma_T$  is the Thomson scattering cross section,  $m_e$  is the electron mass,  $x \equiv r/r_{500}$  with  $r$  being the radial distance to the center of the halo,  $r_{500}$  the radius of a sphere containing the over-density mass  $M_{500c}$  of 500 times the critical density of the universe, and  $\ell_{500} \equiv d_A/r_{500}$ . The integral in Eq. (3) is performed with Romberg's method between  $x_{\min} = 10^{-6}$  and  $x_{\max} = 10$ .

For the pressure profile, we use a standard generalized Navarro-Frenk-White parametrization:

$$P_e(x) = C \times P_0 (c_{500} x)^{-\gamma} [1 + (c_{500} x)^\alpha]^{(\gamma-\beta)/\alpha}, \quad (4)$$

where  $\{\gamma, \alpha, \beta, P_0, c_{500}\}$  are set to their best-fitting values obtained by Planck Collaboration (2013a). The reader is referred to Appendix D of Komatsu et al. (2011) for further details regarding this parameterization. We do not vary these parameters in this paper, which allows us to speed up our likelihood analysis by tabulating  $y_\ell$ . The coefficient  $C$  depends on mass as

$$C = 1.65 \left(\frac{h}{0.7}\right)^2 \left(\frac{H}{H_0}\right)^{\frac{8}{3}} \left[\frac{(h/0.7)\tilde{M}_{500c}}{3 \times 10^{14} M_\odot}\right]^{\frac{2}{3}+0.12} \text{eV cm}^{-3}. \quad (5)$$

The mass used in Eq. (5),  $\tilde{M}_{500c}$ , is not necessarily the true mass but may contain a bias due to non-thermal pressure, observational effects, etc. To account for a possible bias, we relate the true mass to  $\tilde{M}_{500c}$  as  $\tilde{M}_{500c} = M_{500c}/B$ . In the literature, a different variable  $b$  is often used (Planck Collaboration 2013b), and it is related to  $B$  via  $B = (1-b)^{-1}$ . Note that this rescaling not only affects the normalisation of the pressure profile but also its scale dependence via  $\ell_{500}$  because it modifies  $r_{500} \propto M_{500c}^{1/3}$ .

<sup>1</sup> website: [https://github.com/borissbolliet/class\\_sz\\_public](https://github.com/borissbolliet/class_sz_public)

The HMF in Eq. (1) depends on both mass and redshift and is written as

$$\frac{dn}{d \ln M} = -\frac{1}{2} f(\sigma, z) \frac{\rho_{m0}}{M} \frac{d \ln \sigma^2}{d \ln M}, \quad (6)$$

where  $\rho_{m0}$  is the present-day mean mass density of the Universe,  $\sigma^2$  is the variance of the matter over-density field smoothed by a sphere of radius  $R \equiv [3M/4\pi\rho_{m0}]^{1/3}$ , i.e.,

$$\sigma^2(M, z) \equiv \int_{k_{\min}}^{k_{\max}} \frac{dk}{k} \frac{k^3}{2\pi^2} P(k, z) W^2(kR), \quad (7)$$

where  $P(k)$  is the linear matter power spectrum, with  $k_{\min} = 10^{-4} \text{ hMpc}^{-1}$  and  $k_{\max} = 50 \text{ hMpc}^{-1}$ ,  $W$  is the three dimensional Fourier transform of a top-hat window function and  $f(\sigma, z)$  is often measured from N-body simulations. We shall specify the form of  $f(\sigma, z)$  later.

Since the HMF is generally parameterized in terms of the over-density mass  $M_X$ , we write

$$\frac{dn}{d \ln M} = \frac{d \ln M_X}{d \ln M} \frac{dn}{d \ln M_X} = -\frac{d \ln M_X}{d \ln M} \frac{1}{8\pi R_X^3} \frac{d \ln \sigma^2}{d \ln R_X} f(\sigma, z)$$

with  $R_X \equiv [3M_X/4\pi\rho_{m0}]^{1/3}$ , and use an approximation  $d \ln M_X/d \ln M \approx 1$  (see, e.g., Komatsu & Seljak 2001).

We have implemented four different parameterisations of the HMF: the Bocquet et al. (2016) fitting formula obtained from the Magneticum simulation with the impact of baryons; the Tinker et al. (2008) formula; the Tinker et al. (2010) formula, an updated version of the former; the Jenkins et al. (2001) formula. In particular, the Bocquet et al. (2016) and Tinker et al. (2008) HMFs are expressed as

$$f(\sigma, z) = A \left[ \left( \frac{\sigma}{b} \right)^{-a} + 1 \right] \exp \left( -\frac{c}{\sigma^2} \right). \quad (8)$$

The Tinker et al. (2010) HMF is parameterized as

$$f(\nu, z) = \alpha \left[ (\beta^2 \nu)^{-\phi} + 1 \right] \nu^\eta \exp \left( -\gamma \frac{\nu}{2} \right) \sqrt{\nu}, \quad (9)$$

where  $\nu$  is defined via  $\sigma = 1.685/\sqrt{\nu}$ . The fitting parameters of these HMFs depend on redshift and are reported in table 1. The Jenkins et al. (2001) formula for the HMF evaluated at  $M_{180m}$  (over-density mass of 180 times the mean matter density) does not have an explicit redshift dependence and reads as  $f(\sigma) = 0.301 \exp(-|0.64 - \ln \sigma|^{3.82})$ .

The HMF is often given for various over-density masses  $M_X$ . This could be, e.g.,  $M_{200m}$  (over-density mass of 200 times the mean matter density),  $M_{180m}$  or  $M_{500c}$ . There have been two approaches to treat the differences in the mass definitions:

(i) Planck Collaboration (2015); Salvati et al. (2017); Hurier & Lacasa (2017) use  $M_{500c}$  in the integral of Eq. (1). Then, no conversion is needed to compute the pressure profile which often takes  $M_{500c}$  as an input. For the HMF they used Tinker et al. (2008) which provides fitting formulae for various over-density masses with respect to the mean mass density, but not for the critical over-density mass  $M_{500c}$ ; thus, using tables 2 and B3 of the reference they interpolated the HMF parameters at  $M_{500c}$  at every redshift.

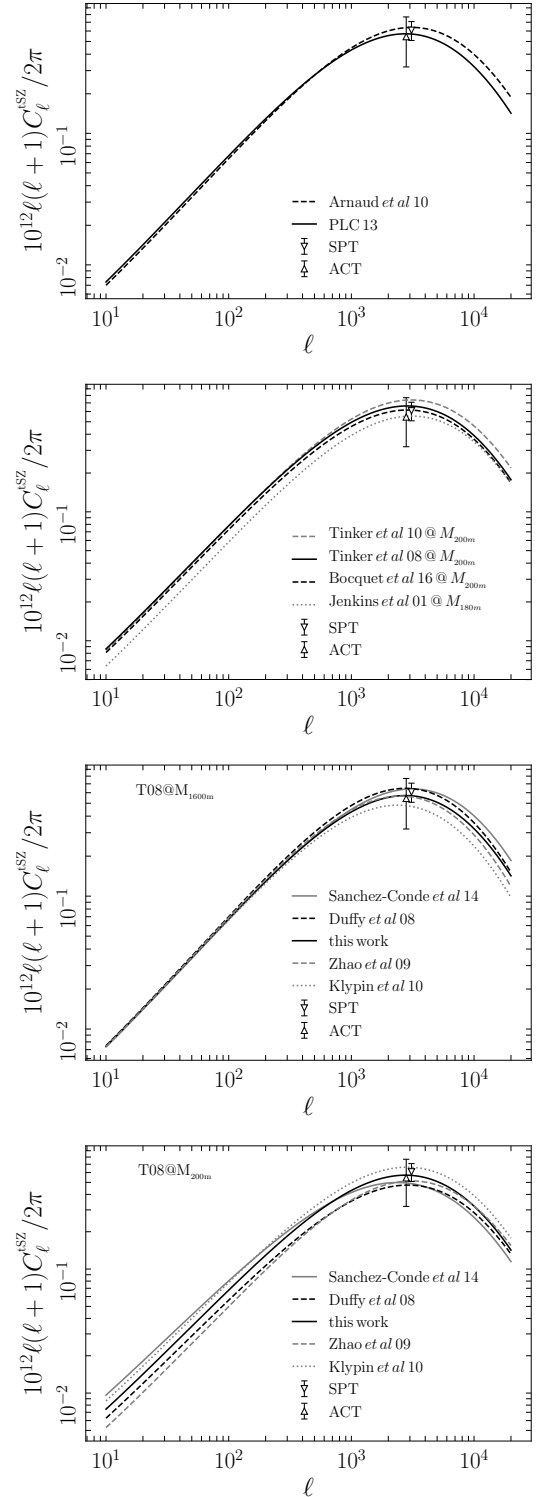


**Figure 1.** tSZ power spectra computed with various settings. From top to bottom panels we show two pressure profiles; four HMFs evaluated at  $M_{200m}$  or  $M_{180m}$  with mass conversion done by the Klypin et al. 2010 concentration-mass relation; the Tinker et al. (2008) HMF (T08) evaluated at  $M_{1600m}$  with mass conversion done by four concentration-mass relations; and same but for  $M_{200m}$ . The solid black lines in the bottom two panels are computed with the Tinker et al. (2008) HMF evaluated at  $M_{500c}$ , so that no mass conversion is needed. The fiducial model is  $\Lambda$ CDM with  $\sigma_8 = 0.79$ ,  $\Omega_m = 0.32$ ,  $h = 0.66$ ,  $B = 1.53$  and  $n_s = 0.81$ . The Atacama Cosmology Telescope (ACT; Hasselfield et al. 2013) and South Pole Telescope (SPT; George et al. 2015) data points are shown for comparison.

(ii) The papers that follow [Komatsu & Seljak \(2002\)](#) use the virial mass  $M_{\text{vir}}$  in the integral of Eq. (1). Conversion from the virial mass to the over-density mass is needed twice: for the HMF and for the pressure profile. The conversion is carried out using the so-called concentration-mass relation for dark matter halos. We have implemented four concentration-mass relations, including [Duffy et al. \(2008\)](#), i.e.,  $c_{\text{vir}} = 7.85 \times (M_{\text{vir}}/2 \times 10^{12})^{-0.81} \times (1+z)^{-0.71}$ , where  $M_{\text{vir}}$  is in units  $h^{-1}M_{\odot}$ ; [Klypin et al. \(2011\)](#), i.e.,

$$c_{\text{vir}} = c_0 \times (M_{\text{vir}}/10^{12})^{-0.075} \times [1 + (M_{\text{vir}}/M_0)^{-0.26}],$$

where  $c_0$  and  $M_0$  are functions of redshift and whose tabulation can be found in table 3 of the reference; [Sánchez-Conde & Prada \(2014\)](#), which uses concentrations at the over-density mass  $M_{200c}$  of 200 times the critical density of the universe instead of  $M_{\text{vir}}$ , i.e.,  $c_{200} = \sum_{i=0}^5 c_i \times [\ln(M_{200c})]^i \times (1+z)^{-1}$ , where the values for the coefficients  $c_i$  are given below Eq. 1 of the reference; and [Zhao et al. \(2009\)](#) which does not give an explicit concentration-mass relation but computes it numerically at every redshift with the `mandc` code<sup>2</sup>. In this case, we ran `mandc` for the Planck 2015 best-fitting cosmological parameters and for several redshift values and tabulated the concentration for subsequent interpolation.

The original motivation behind the second approach was that the HMF was thought to be more universal (i.e., the function  $f(\sigma, z)$  is a function of  $\sigma$  only, without explicit dependence on  $z$ ) when using  $M_{200m}$ . However, [Tinker et al. \(2008\)](#) showed that the HMF is not universal for any masses. This then motivates the first approach, which calibrates the HMF directly for the relevant mass definition for the pressure profile, such as  $M_{500c}$ . These two strategies have led to different conclusions regarding the cosmological parameter constraints obtained from the SZ power spectrum data. In particular, the work based on the second approach has found a higher value of  $\sigma_8$  than the Planck Collaboration that uses the first approach, by about two standard deviations. Here we show that this discrepancy is not due to the use of different HMFs, but to the ambiguity of the use of the concentration-mass relation.

In figure 1 we show the tSZ power spectra computed with different settings. In the top panel we compare the power spectra using the Planck pressure profile and that of the original work by [Arnaud et al. \(2010\)](#). They make little difference at  $\ell \lesssim 10^3$ . In the second panel we compare the spectra using the four halo mass functions (HMFs). While the [Jenkins et al. \(2001\)](#) HMF gives somewhat lower amplitude, the others give similar results. In the third panel we compare the spectra using the [Tinker et al. \(2008\)](#) HMF for  $M_{1600m}$  (which is close to  $M_{500c}$ ) and the four concentration-mass relations. We find that all concentration-mass relations give similar results at  $\ell \lesssim 10^3$  because conversion from  $M_{500c}$  to  $M_{1600m}$  is small. However, in the last panel the four concentration-mass relations give diverging results because we use the [Tinker et al. \(2008\)](#) HMF for  $M_{200m}$ . In particular, the [Duffy et al. \(2008\)](#) concentration-mass relation leads to an underestimation of the tSZ power compared to the third panel. So, to fit the same data, tSZ power spectrum models with [Duffy et al. \(2008\)](#) concentration-mass relation

Parameter	Min.	Max.
$10^9 A_s$	1.8	2.7
$n_s$	0.8	1
$\tau_{\text{reio}}$	0.04	0.12
$100\theta_s$	1.03	1.05
$\Omega_b h^2$	0.0199	0.0245
$\Omega_c h^2$	0.09	0.15
$w$	-2	-0.5
$B$	1.11	1.67
$A_{\text{CIB}}$	0	10
$A_{\text{IR}}$	0	10
$A_{\text{RS}}$	0	10

**Table 2.** Uniform priors on parameters of the MCMC analysis.

and  $M_{200m}$  need a larger  $\sigma_8$  than models without mass conversion. In other words, using the approach of [Komatsu & Seljak \(2002\)](#) with the [Duffy et al. \(2008\)](#) concentration-mass relation for the mass conversion would lead to an over-estimation of  $\sigma_8$ .

### 3 WHAT DETERMINES THE AMPLITUDE OF THE POWER SPECTRUM?

In figure 2, we show how the cosmological parameters and the mass bias affect the tSZ power spectrum, computed with the [Tinker et al. \(2008\)](#) HMF evaluated at  $M_{500c}$  so that no mass conversion is needed. When we vary  $h$ ,  $\Omega_m$ ,  $w$ , and  $n_s$ , we hold  $\sigma_8$  fixed by adjusting the primordial scalar amplitude parameter  $A_s$ . For the multipole range of interest ( $\ell < 10^3$ ), the EoS of dark energy  $w$  (bottom middle panel) and the spectral index  $n_s$  (bottom right panel) have a minor effect on the amplitude of the tSZ power spectrum, in agreement with [Komatsu & Seljak \(2002\)](#). The mass bias  $B$  as well as  $h$ ,  $\sigma_8$ , and  $\Omega_m$  affect the amplitude of the power spectrum significantly. We find that the scaling of the power spectrum is well approximated by

$$C_{\ell}^{\text{tSZ}} \propto \sigma_8^{8.1} \Omega_m^{3.2} B^{-3.2} h^{-1.7} \quad \text{for } \ell \lesssim 10^3. \quad (10)$$

The dependence on  $\sigma_8$  and  $\Omega_m$  agrees with that of [Planck Collaboration \(2015\)](#). We now add extra dependence on  $B$  and  $h$ . We can understand the dependence on  $B$  approximately by looking at how  $y_{\ell}$  at small multipoles scales as  $B$ , i.e.,  $y_{\ell} \propto r_{500c}^3 M_{500c}^{2/3+0.12}$ , which gives  $C_{\ell}^{\text{tSZ}} \propto B^{-3.6}$ . In this paper we simplify Eq. (10) as

$$F \equiv \sigma_8 (\Omega_m/B)^{0.40} h^{-0.21}, \quad (11)$$

and find a constraint on  $F$ .

### 4 MAXIMUM LIKELIHOOD ANALYSIS

We derive cosmological constraints from the power spectrum of the [Planck Collaboration \(2015\)](#) Compton  $y$  map. To this end we sample the parameter space by the Markov Chain Monte Carlo (MCMC) method and extract joint posterior probability distributions of the parameters.

We use the effective multipole range of  $10 \leq \ell_{\text{eff}} \leq 959.5$ . The effective multipoles are defined to be the middle of the eighteen bins spanning this interval and used in the [Planck Collaboration \(2013b\)](#) and [Planck Collaboration \(2015\)](#) (PLC15) tSZ analyses.

<sup>2</sup> website: <http://202.127.29.4/dhzhao/mandc.html>



$\ell_{\text{eff}}$	$10^{12} \hat{D}_\ell^{y^2}$	$\sigma_\ell^{y^2}$	$10^{12} \hat{D}_\ell^{\text{RC}}$	$\sigma_\ell^{\text{RC}}$	$10^{12} \hat{D}_\ell^{\text{CIB}}$	$10^{12} \hat{D}_\ell^{\text{RS}}$	$10^{12} \hat{D}_\ell^{\text{IR}}$	$10^{12} \hat{D}_\ell^{\text{CN}}$
10	0.00508	0.00629	0.000421	0.000160	0.000000	0.000043	0.000007	0.000001
13.5	0.00881	0.00615	0.000710	0.000192	0.000000	0.000142	0.000024	0.000001
18	0.01363	0.00579	0.001251	0.000254	0.000000	0.000296	0.000048	0.000002
23.5	0.02961	0.00805	0.002837	0.000446	0.000000	0.000400	0.000073	0.000004
30.5	0.02241	0.00521	0.003933	0.000460	0.000902	0.000541	0.000111	0.000006
40	0.02849	0.00464	0.005969	0.000510	0.002010	0.001056	0.000224	0.000010
52.5	0.04276	0.00468	0.010318	0.000672	0.003119	0.001647	0.000449	0.000018
68.5	0.04580	0.00429	0.014045	0.000699	0.006278	0.002787	0.000837	0.000030
89.5	0.07104	0.00454	0.024061	0.000896	0.012242	0.004306	0.001400	0.000052
117	0.11914	0.00562	0.032976	0.000936	0.021584	0.006842	0.002701	0.000089
152.5	0.15150	0.00594	0.047100	0.001020	0.045915	0.011264	0.004721	0.000153
198	0.19390	0.00611	0.062380	0.001040	0.070582	0.016744	0.008115	0.000262
257.5	0.28175	0.00687	0.081730	0.001030	0.119786	0.027345	0.014618	0.000456
335.5	0.39837	0.00824	0.101911	0.000978	0.211686	0.043275	0.024893	0.000815
436.5	0.56743	0.00958	0.117412	0.000860	0.332863	0.070587	0.051570	0.001503
567.5	0.76866	0.01242	0.132234	0.000769	0.434931	0.115356	0.107293	0.002934
738	1.11010	0.01650	0.143214	0.000642	0.602030	0.154926	0.197053	0.006334
959.5	1.66140	0.02400	0.156202	0.000544	0.754733	0.207200	0.361713	0.016171
1247.5	2.52170	0.04170	0.175341	0.000492	1.029014	0.287652	0.681036	0.054883
1622	4.58510	0.09870	0.283969	0.000900	1.357567	0.410274	1.295272	0.301480
2109	12.2690	0.40100	1.363680	0.003650	1.850146	0.657659	2.534448	3.738250
2742	165.600	23.6000	54.69000	2.310000	2.629002	1.117189	4.545315	183.2673

**Table 3.** Planck 2015 data points and Gaussian error bars of the  $y^2$  power spectrum  $\hat{C}_\ell^{y^2}$ , the tSZ power spectrum from resolved clusters  $\hat{C}_\ell^{\text{RC}}$ , and templates for the foreground contributions: CIB, IR, and RS. The last column is the power spectrum of correlated noise (CN). These data were taken from [Planck Collaboration \(2015\)](#). Note that we used  $D_\ell \equiv [\ell(\ell+1)/2\pi]C_\ell$ .

We assume a flat universe and the standard number of neutrino species  $N_{\text{eff}} = 3.046$ , with  $\Sigma m_\nu = 0.06$  eV. Although neutrinos play an important role on non-linear scales because they slow down gravitational collapse, we ignore their effect on the halo mass function in this paper (as was done in the Planck SZ analyses). Given the low value of the neutrino mass we consider, this is an acceptable approximation: a careful treatment would affect the determination of  $F$  by less than one percent, see [Costanzi et al. \(2013\)](#).

We vary  $B$ ,  $A_s$ ,  $n_s$ , and  $w$ , as well as the optical depth to electron scattering during re-ionisation  $\tau_{\text{reio}}$ , the angular size of the sound horizon at decoupling  $\theta_s$ , the baryon density  $\Omega_b h^2$ , the cold dark matter density  $\Omega_c h^2$ , and the nuisance parameters ( $A_{\text{CIB}}$ ,  $A_{\text{IR}}$ ,  $A_{\text{RS}}$ ) that will be described below. The other parameters,  $h$ ,  $\sigma_8$ , and  $\Omega_m$ , are derived parameters.

We split these parameters into the so-called ‘‘fast’’ and ‘‘slow’’ parameters as

$$\underbrace{A_s, n_s, \tau_{\text{reio}}, \theta_s, \Omega_b h^2, \Omega_c h^2, w, B}_{C_\ell^{\text{SZ}}: \text{slow param.}}, \underbrace{A_{\text{CIB}}, A_{\text{IR}}, A_{\text{RS}}}_{C_\ell^{\text{FG}}: \text{fast param.}}. \quad (12)$$

This splitting makes MCMC exploration of the parameter space efficient ([Lewis 2013](#)). We use [Montepython \(Audren et al. 2013\)](#) for the sampling. We impose weak uniform priors on the parameters to avoid unrealistic regions of the parameter space. See table 2 for the priors we adopt. The prior on the mass bias  $B$  is motivated by the scatter of the results from numerical simulations (it corresponds to  $0.1 < b < 0.4$ ). For the other parameters, the allowed range is wide enough so that changing the upper or lower bound does not affect our posterior likelihood.

We start by fitting the *total* power spectrum of the Compton  $y$  map,  $\hat{C}_\ell^{y^2}$ , which includes contributions from tSZ, three foreground components (the cosmic infrared back-

ground (CIB), radio sources (RS) and infrared point sources (IR)), and a correlated noise (CN) term. Our model is

$$C_\ell^{y^2} = C_\ell^{\text{tSZ}} + A_{\text{CIB}} \hat{C}_\ell^{\text{CIB}} + A_{\text{IR}} \hat{C}_\ell^{\text{IR}} + A_{\text{RS}} \hat{C}_\ell^{\text{RS}} + A_{\text{CN}} \hat{C}_\ell^{\text{CN}}, \quad (13)$$

where  $\hat{C}_\ell^{\text{CIB}}$ ,  $\hat{C}_\ell^{\text{IR}}$ ,  $\hat{C}_\ell^{\text{RS}}$ , and  $\hat{C}_\ell^{\text{CN}}$  are templates of the foreground and correlated noise terms, respectively (see table 3). Since the correlated noise term dominates over the other terms at high multipoles, we use the highest multipole data at  $\ell = 2742$  to determine  $A_{\text{CN}}$ , i.e.,  $A_{\text{CN}} = \hat{C}_{2742}^{y^2} / \hat{C}_{2742}^{\text{CN}} = 0.903$ . We then fit for and marginalise over the amplitudes of the foreground term,  $A_{\text{CIB}}$ ,  $A_{\text{IR}}$ ,  $A_{\text{RS}}$ .

In fact, there is a physical upper bound on the total foreground power; namely, the sum of the tSZ power from *resolved* sources<sup>3</sup>  $\hat{C}_\ell^{\text{RC}}$  and the total foreground power cannot exceed the  $\hat{C}_\ell^{y^2}$  data. Thus,

$$A_{\text{CIB}} \hat{C}_\ell^{\text{CIB}} + A_{\text{IR}} \hat{C}_\ell^{\text{IR}} + A_{\text{RS}} \hat{C}_\ell^{\text{RS}} + A_{\text{CN}} \hat{C}_\ell^{\text{CN}} < \hat{C}_\ell^{y^2} - \hat{C}_\ell^{\text{RC}}. \quad (14)$$

We use this upper bound as follows. At each step of the MCMC, we ensure that the foreground amplitudes  $\{A_{\text{CIB}}, A_{\text{IR}}, A_{\text{RS}}\}$  satisfy Eq. (14) in the seven multipole bins between  $\ell_{\text{eff}} = 257.5$  and 1247.5; the proposed step in the MCMC is rejected otherwise. This multipole range is chosen because above  $\ell_{\text{eff}} = 1247.5$   $\hat{C}_\ell^{\text{RC}}$  is significantly affected by the resolution of the  $y$ -map, while below  $\ell_{\text{eff}} = 257.5$ , statistical and systematic uncertainties are important and Eq. (14) is no longer applicable.

<sup>3</sup> The data for  $\hat{C}_\ell^{\text{RC}}$  and the error bars  $\sigma_\ell^{\text{RC}}$  are also reported in table 3 (see [Planck Collaboration 2013b, 2015](#), for details).

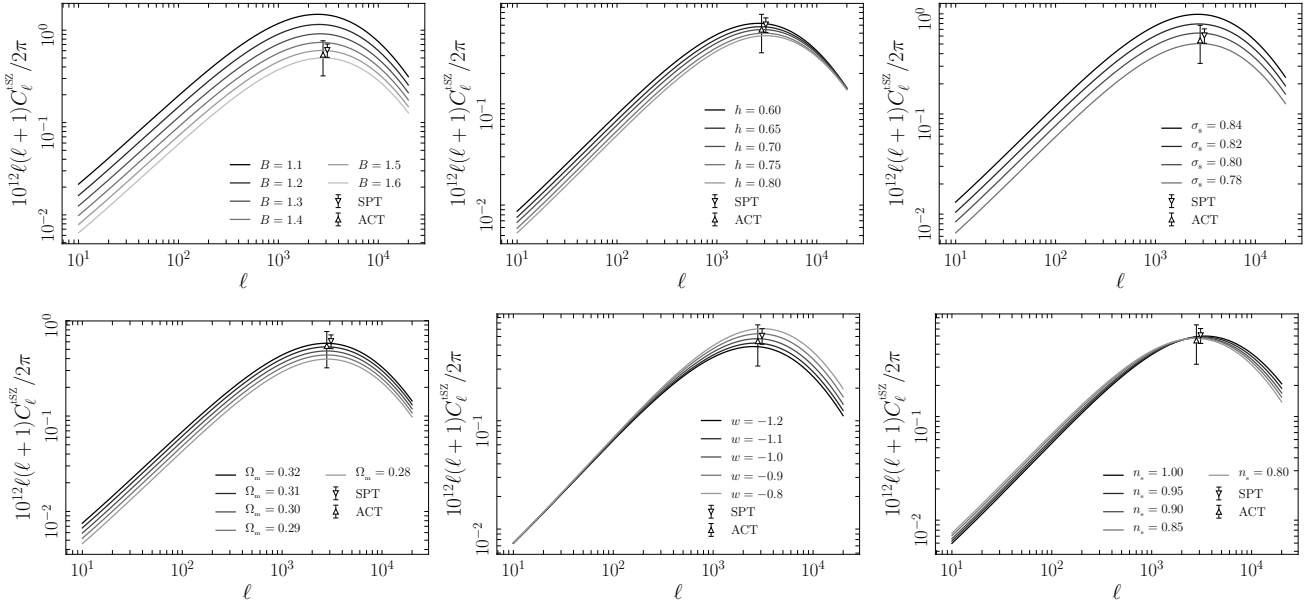


**Figure 2.** Dependence of the tSZ power spectrum on the mass bias  $B$  as well as on the cosmological parameters  $h$ ,  $\sigma_8$ ,  $\Omega_m$ ,  $w$ , and  $n_s$ . We hold  $\sigma_8$  fixed by adjusting the primordial scalar amplitude parameter  $A_s$  in all but the top-left and top-right panels. The fiducial model is the same as in figure 1.

The likelihood is computed according to  $-2 \ln \mathcal{L} = \chi^2 + \ln |M| + \text{const.}$  with

$$\chi^2 \equiv \sum_{a \leq a'} \left( C_{\ell_{\text{eff}}^a}^{y^2} - \hat{C}_{\ell_{\text{eff}}^a}^{y^2} \right) [M^{-1}]_{aa'} \left( C_{\ell_{\text{eff}}^{a'}}^{y^2} - \hat{C}_{\ell_{\text{eff}}^{a'}}^{y^2} \right), \quad (15)$$

where  $a, a'$  are indices for the multipole bins running from  $a = 1$  to  $a = 18$ ,  $C_{\ell_{\text{eff}}^a}^{y^2}$  is given by Eq. (13),  $\hat{C}_{\ell_{\text{eff}}^a}^{y^2}$  are the data points,  $M$  is the binned covariance matrix, and  $|M|$  is its determinant. The elements of the binned covariance matrix are

$$M_{aa'} = \left( \sigma_{\ell_{\text{eff}}^a}^{y^2} \right)^2 \delta_{aa'} + \frac{\ell_{\text{eff}}^a (\ell_{\text{eff}}^a + 1) \ell_{\text{eff}}^{a'} (\ell_{\text{eff}}^{a'} + 1)}{4\pi^2} \frac{T_{aa'}}{4\pi f_{\text{sky}}}, \quad (16)$$

where  $\sigma_{\ell_{\text{eff}}^a}^{y^2}$  are the measured error bars (third column of table 3) which comes from both the sampling variance and Gaussian instrumental noise,  $f_{\text{sky}} = 0.47$  is the Planck sky coverage, and  $T_{aa'}$  is the binned trispectrum given by

$$T_{aa'} = \sum_{\ell \in a} \sum_{\ell' \in a'} \frac{T_{\ell\ell'}}{N_a N_{a'}}, \quad (17)$$

where  $a$  and  $a'$  denote two multipole bins containing respectively  $N_a$  and  $N_{a'}$  multipoles. The unbinned trispectrum  $T_{\ell\ell'}$  is assumed to be dominated by the tSZ effect contribution. We follow Komatsu & Seljak (2002) and calculate

$$T_{\ell\ell'} = \int dz \frac{dV}{dz d\Omega} \int d \ln M \frac{dn}{d \ln M} |y_\ell(M, z)|^2 |y_{\ell'}(M, z)|^2, \quad (18)$$

where the redshift and mass ranges are the same as for the power spectrum, see Eq. (1).

In the left panel of figure 3 we compare the trispectrum and Gaussian contributions to the covariance matrix. As found by Komatsu & Seljak (2002), the trispectrum dominates over the Gaussian term at low multipoles (when

binned linearly in multipoles). This is due to large massive halos at low redshift covering a large fraction of the sky. Adding a few large halos in the sky increase the tSZ power significantly at many multipoles, producing a large multipole-to-multipole correlation. We find that the binned and unbinned trispectra are similar; thus, to save computational time we use the unbinned trispectra evaluated at  $\ell_{\text{eff}}$ .

As both the power spectrum and trispectrum depend on the cosmological parameters, we compute them at each step of the MCMC sampling. In principle, we would also need to vary the Gaussian term of the covariance matrix at each step; however, since the total variance is dominated by the trispectrum at low multipoles and by Gaussian instrumental noise at high multipoles, we use the values derived by the PLC15 analysis.

## 5 RESULTS

In subsection 5.1 we compare constraints on  $F$  with and without trispectrum in the covariance matrix. In subsection 5.2 we obtain the mass bias that reconciles the tSZ and primary CMB data within the context of  $\Lambda$ CDM. Finally, in subsection 5.3 we present our results on dark energy.

### 5.1 Constraints on $F$

To illustrate importance of the trispectrum, we first obtain a constraint on  $F$  without it. Marginalising over all the relevant cosmological, foreground, and mass bias parameters, we find  $F = 0.473 \pm 0.005$  (68% CL). When the trispectrum is included, the 68% C.L. error bar increases by a factor of more than two. We find  $F = 0.460 \pm 0.012$  (68% CL), and  $A_{\text{CIB}} = 0.53 \pm 0.16$ ,  $A_{\text{IR}} = 2.05 \pm 0.18$ ,  $A_{\text{RS}} = 0.34_{-0.34}^{+0.07}$ .

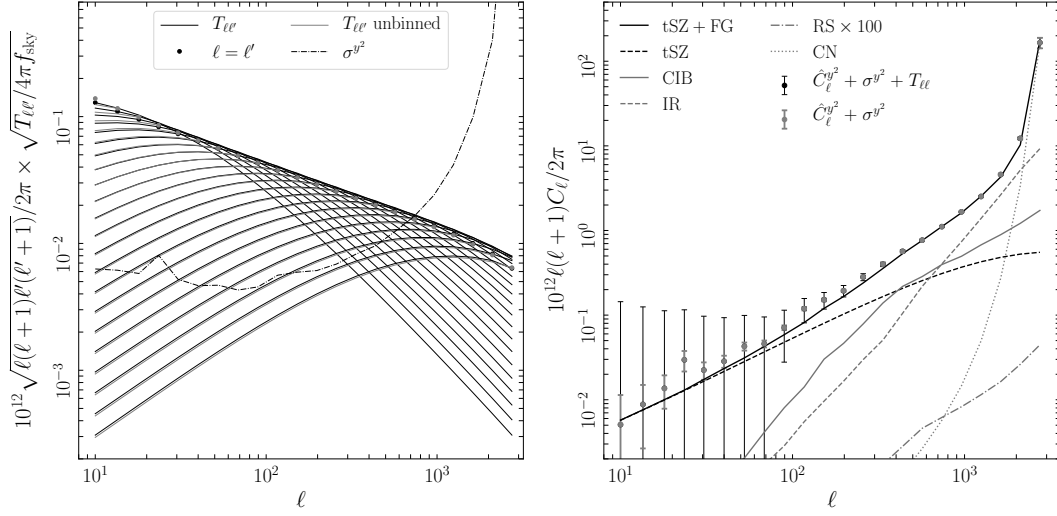


**Figure 3.** (Left panel) tSZ power spectrum covariance matrix, for the multipole values  $\ell_{\text{eff}}$  listed in table 4. The dot-dashed line shows the Gaussian term  $\sigma_{\ell}^{y^2}$ , while the thick and thin solid lines show the binned and unbinned trispectrum terms  $10^{12} \sqrt{\ell(\ell+1)\ell'(\ell'+1)/4\pi^2} \times \sqrt{T_{\ell\ell'}/4\pi f_{\text{sky}}}$ , respectively (see Eq.(16)). The filled circles show the diagonals of the trispectrum, and the lines show off-diagonal terms. (Right panel) The best-fitting tSZ (black dashed line), CIB (grey solid), IR (grey dashed), RS (times 100; dot-dashed), and correlated noise (CN; dotted) power spectra. The black solid line shows the sum of all the components. The filled circles show the data points used in this work, with the Gaussian and total diagonal elements of the covariance matrix shown in the grey and black error bars, respectively. The parameters of the best-fitting model are:  $\sigma_8 = 0.78$ ,  $\Omega_m = 0.31$ ,  $h = 0.69$ ,  $B = 1.41$  (i.e.,  $F = 0.460$ ),  $n_s = 0.96$ ,  $A_{\text{CIB}} = 0.66$ ,  $A_{\text{IR}} = 2.04$ , and  $A_{\text{RS}} = 0.0004$ .

In the right panel of figure 3 we show the best-fitting power spectra of the tSZ and foregrounds, as well as the original  $\hat{C}_{\ell}^{y^2}$  data points. We show the correlations among  $F$  and foreground parameters in figure 4. In the left panel of figure 5 we show the derived tSZ power spectrum data points (with the foregrounds subtracted and marginalised over; black points, see table 4 for the data). In the right panel of figure 5 we compare our derived tSZ power with those of the PLC15 (grey points) and the ACT (Hasselfield et al. 2013) and SPT (George et al. 2015) measurements at  $\ell = 3000$ . Our tSZ data points at  $\ell \gtrsim 300$  are significantly smaller than the PLC15, and we attribute this difference to our including the trispectrum in the analysis. We also show the tSZ power spectrum computed from the **Magneticum** simulation (Dolag et al. 2016) with  $\Omega_m = 0.308$ ,  $\sigma_8 = 0.815$ ,  $h = 0.704$ ,  $n_s = 0.963$ , and  $\Omega_b = 0.0456$ . While this power spectrum agrees well with the PLC15 data points, as claimed by the authors, our best-fitting model is approximately 2/3 of their power spectrum.

## 5.2 Mass bias in $\Lambda$ CDM

Given a cosmological model, we can constrain the mass bias  $B$  by combining the tSZ likelihood with the Planck CMB data. Assuming a flat  $\Lambda$ CDM and using the Planck CMB “TT+lowP” chains (Planck Collaboration 2016a), we find  $\sigma_8 \Omega_m^{0.40} h^{-0.21} = 0.568 \pm 0.015$  (68% CL). Comparing this to the above constraint on  $F$ , we derive the mass bias as  $B = 1.71 \pm 0.17$  (68% CL), or  $(1-b) = 0.58 \pm 0.06$ .

The origin of this mass bias is not known. It is possible that a part of the bias comes from non-thermal pressure support because  $\tilde{M}_{500c}$  in the universal pressure profile was

$\ell_{\text{eff}}$	$10^{12} D_{\ell}^{\text{tSZ}}$	$\sigma_{\ell}^{\text{tSZ}}$	$10^{12} D_{\ell}^{\text{tSZ}}$ (BF)
10	5.0496e-03	1.3919e-01	5.7234e-03
13.5	8.7080e-03	1.1643e-01	7.5606e-03
18	1.3430e-02	9.9155e-02	9.9280e-03
23.5	2.9325e-02	8.6276e-02	1.2834e-02
30.5	2.1520e-02	7.4827e-02	1.6544e-02
40	2.6605e-02	6.4972e-02	2.1591e-02
52.5	3.9626e-02	5.6584e-02	2.8250e-02
68.5	3.9820e-02	4.9513e-02	3.6721e-02
89.5	6.0241e-02	4.3516e-02	4.7775e-02
117	9.9878e-02	3.8669e-02	6.2081e-02
152.5	1.1375e-01	3.4993e-02	8.0185e-02
198	1.3429e-01	3.2630e-02	1.0271e-01
257.5	1.7920e-01	3.3977e-02	1.3093e-01
335.5	2.2076e-01	4.3272e-02	1.6575e-01
436.5	2.6166e-01	6.0483e-02	2.0728e-01
567.5	2.7879e-01	7.9377e-02	2.5553e-01
738	3.3226e-01	1.1034e-01	3.0982e-01
959.5	4.3979e-01	1.4774e-01	3.6810e-01
1247.5	–	–	4.2699e-01
1622	–	–	4.8154e-01
2109	–	–	5.2553e-01
2742	–	–	5.5249e-01

**Table 4.** tSZ power spectrum and total uncertainties with the foreground and correlated noise power spectra marginalised over. The last column is the best-fitting tSZ power spectrum (see right panel of figure 5). Note that we used  $D_{\ell} \equiv [\ell(\ell+1)/2\pi]C_{\ell}$ .

derived assuming hydrostatic equilibrium with thermal gas pressure (Arnaud et al. 2010). However, the value of  $B$  we find appears to be significantly larger than expected from both analytical calculations and some numerical simulations (e.g., Shi & Komatsu 2014; Shi et al. 2015, and references therein), but see Henson et al. (2017) for the simulation

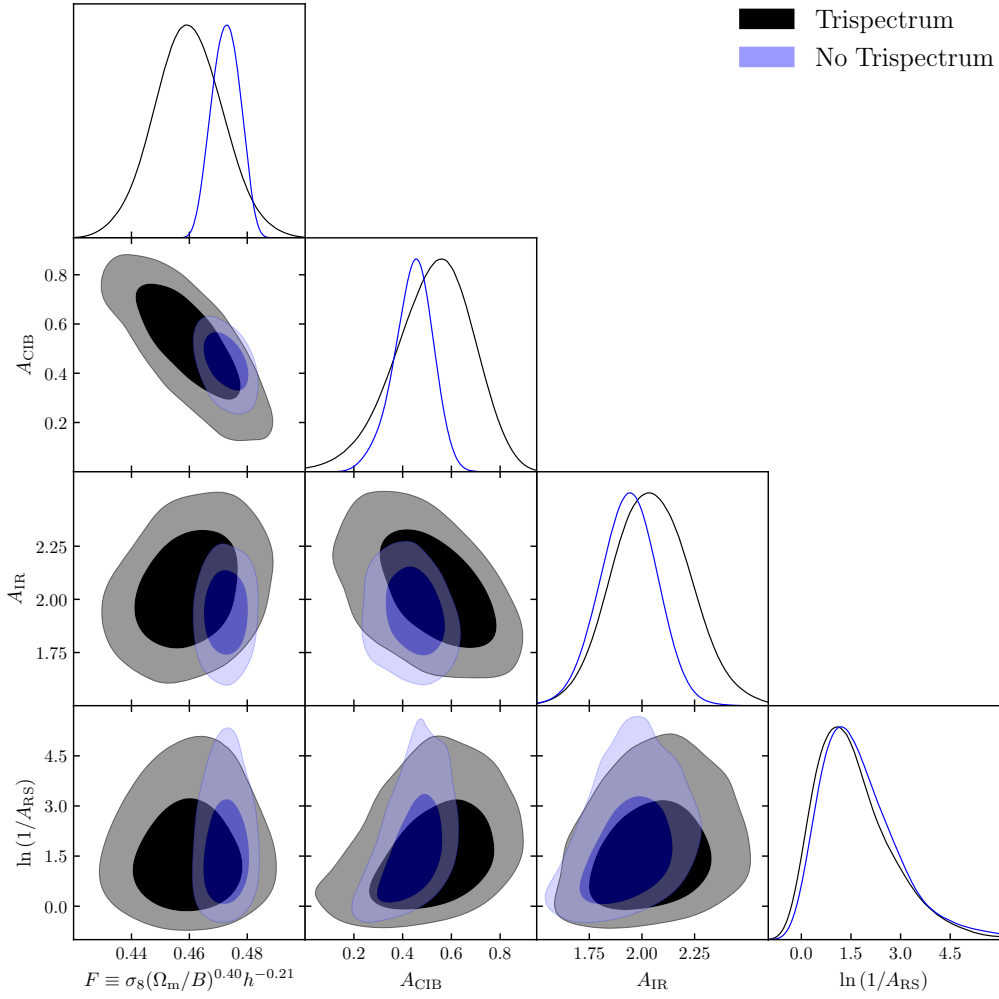


**Figure 4.** Marginalised (1D and 2D) joint posterior probability distributions of the  $F$ -parameter (Eq. (11)) and the foreground amplitudes (CIB, IR, and RS). The black and blue contours show the results with and without trispectrum in the covariance, respectively.

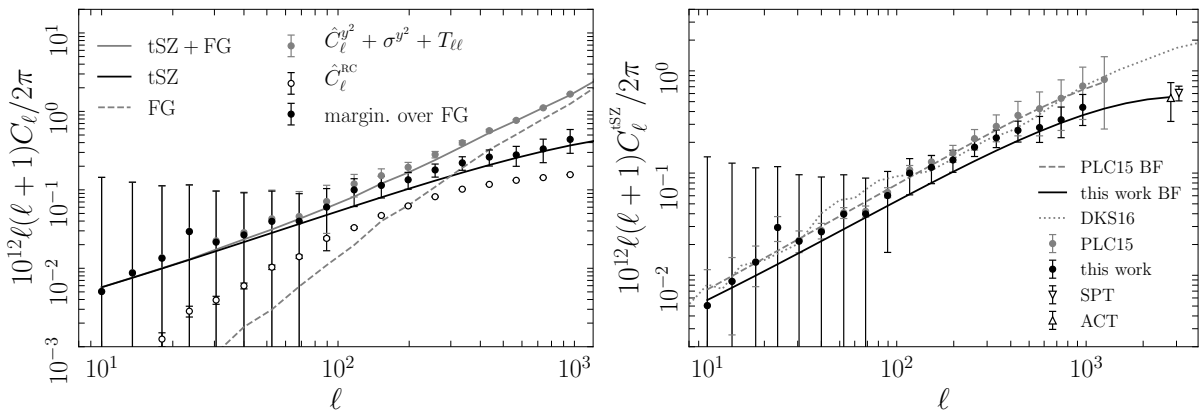


**Figure 5.** (Left panel) Best-fitting tSZ (solid black line) and total foreground (dashed line) power spectra. The solid grey line shows their sum. The open circles show the contribution from resolved clusters. The grey circles show the original data points with error bars including the trispectrum, whereas the black filled circles show the data points with the foreground spectra marginalised over. (Right panel) The black line and circles are the same as those in the left panel. See figure 3 for the best-fitting model parameters, and table 4 for the tabulated values. The grey circles show the foreground-marginalised data points obtained by the Planck 2015 SZ analysis. We also show the ACT and SPT data points for comparison, as well as the simulation results of Dolag et al. (2016) (DKS16, grey dotted line).



work pointing towards a larger mass bias. It is also possible that hydrostatic equilibrium does not hold even when we add both thermal and non-thermal pressure, though this is not expected to be significant for  $M_{500c}$  (Lau et al. 2009). Finally, the bias may be due to non-physical effects such as instrumental and analysis systematics of the X-ray data used to derive  $\bar{M}_{500c}$  in the universal pressure profile.

Observationally, the mass bias we find is consistent with a recent weak lensing constraint,  $(1-b) = 0.73 \pm 0.10$  (Penna-Lima et al. 2017), as well as with the Planck tSZ cluster number counts analysis which yields  $(1-b) = 0.58 \pm 0.04$  (Planck Collaboration 2016b).

Alternatively, such a large mass bias required within the context of  $\Lambda$ CDM hints that the mass bias is not a culprit but a modification to  $\Lambda$ CDM, such as dark energy that is different from a cosmological constant, may be needed.

### 5.3 Constraints on Dark Energy

As dark energy slows down structure formation, we can constrain the dark energy EoS  $w$  by comparing the amplitude of fluctuations at  $z = 1090$  measured by the CMB and that in a low redshift universe measured by tSZ. Specifically, the CMB constraint gives  $\sigma_8$  as a function of  $w$ , or  $F$  as a function of  $w$  and  $B$ ; thus, we can trade  $B$  for  $w$ . In this section we constrain  $w$  within the framework of a flat  $w$ CDM model.

The black contours in figure 6 show marginalised joint posterior probability distributions of  $w$ ,  $\sigma_8$ ,  $\Omega_m$ , and  $h$  from the tSZ power spectrum *alone*. As expected we cannot constrain individual parameters using the tSZ power spectrum alone, but a constraint on the parameter  $F$  (Eq. (11)) for  $w$ CDM,  $F = 0.460 \pm 0.013$  (68% CL), is similar to that for  $\Lambda$ CDM.

To constrain  $w$ , we now add to our likelihood some external constraints on the primordial scalar amplitude  $A_s$  and  $h$ . The latter is needed because  $F$  contains  $h$ . We apply a Gaussian prior on  $h = 0.72 \pm 0.03$  from local measurements of the Hubble constant (see Bernal et al. 2016, and references therein). The CMB temperature anisotropy (without CMB lensing) data do not constrain  $A_s$ , but only a combination  $A_s e^{-2\tau_{\text{reio}}}$  because a small fraction of CMB photons from  $z = 1090$  are re-scattered in a reionised universe at  $z \lesssim 20$ . While the exact constraint on  $A_s e^{-2\tau_{\text{reio}}}$  is somewhat model dependent, we follow the procedure of the ‘‘WMAP amplitude prior’’ (Komatsu et al. 2009) to find a robust Gaussian prior on  $10^9 A_s e^{-2\tau_{\text{reio}}} = 1.878 \pm 0.014$  from the Planck 2015 data. See table 5 for summary. Finally, we use a Gaussian prior on the optical depth, motivated by the latest Planck measurement, i.e.,  $\tau_{\text{reio}} = 0.06 \pm 0.01$  (see Calabrese et al. 2017, footnote 1), to obtain a prior on  $A_s$ .

The mass bias also needs to be constrained before we can measure  $w$ . With the flat prior given in table 2,  $1.11 < B < 1.67$ , motivated by the scatter of results from numerical simulations, we find  $w = -1.15 \pm 0.15$  (68% CL). The blue contours in figure 6 show 2d marginalised distributions. If we further assume a fixed value for the mass bias, for instance we assume that *all* of the mass bias is due to non-thermal pressure and take  $B = 1.25$  as in Dolag et al. (2016), we find

$$w = -1.10 \pm 0.12 \text{ (68\% CL)}, \quad (19)$$

as well as  $\sigma_8 = 0.802 \pm 0.037$  and  $\Omega_m = 0.265 \pm 0.022$ .

	$10^9 A_s e^{-2\tau_{\text{reio}}}$
$\Omega_k = 0$ and $w = -1$ . . . . .	$1.880 \pm 0.014$
$\Omega_k \neq 0$ and $w = -1$ . . . . .	$1.872 \pm 0.014$
$\Omega_k = 0$ and $w \neq -1$ . . . . .	$1.880 \pm 0.014$
$\Omega_k = 0$ and $w = -1$ and $m_\nu > 0$	$1.881 \pm 0.014$
Amplitude prior . . . . .	$1.878 \pm 0.014$

**Table 5.** Constraints on  $10^9 A_s e^{-2\tau_{\text{reio}}}$  at  $k = 0.05 \text{Mpc}^{-1}$  from the publicly available Planck 2015 chains assuming four different cosmological models. The last row shows our summary for the amplitude prior.

The yellow contours in figure 6 show 2d marginalised distributions. In particular, the contours in the  $h$ - $w$  plane show a strong correlation. Hence, the central value of our constraint on the EoS depends primarily on the prior on  $h$ . A smaller Hubble parameter would lead to a less negative  $w$ .

How does this ‘‘amplitude-derived’’ constraint on  $w$  compare with a more common ‘‘distance-derived’’ constraint on  $w$ ? To this end we form a compressed likelihood (or a distance prior) of the distance information from CMB data following the previous work (Mukherjee et al. 2008; Komatsu et al. 2009; Wang & Dai 2016). The likelihood includes the shift parameter  $R$  and the angular scale of the sound horizon at last scattering  $\ell_A$ , as well as the baryon density. We emphasise that the compressed likelihood ignores the effect of dark energy on large scale perturbations, i.e., the late integrated Sachs-Wolfe effect, as it uses only the distance information. As a result, the dark energy constraint from the compressed likelihood is slightly weaker than the full analysis (though by not much). A comprehensive discussion on this point can be found in section 5.4 of Komatsu et al. (2009).

At each step of the MCMC, we compute

$$\chi_{\text{CMB}}^2 = \sum_{i,j=1}^3 (P - \bar{P})_i [C^{-1}]_{ij} (P - \bar{P})_j, \quad (20)$$

where  $P \equiv \{R, \ell_A, \Omega_b h^2\}$  contains the proposed values of the parameters and  $\bar{P}$  contains the posterior mean values of the  $w$ CDM ‘‘lowTEB+lensing’’ chains (Planck Collaboration 2016a). The covariance matrix is given by  $C_{ij} = \sigma_i \sigma_j D_{ij}$ . The posterior mean, the standard deviation  $\sigma_i$ , and the correlation matrix  $D_{ij}$  are given in the first three rows of table 6. To this we add a prior on  $h$  from the above, and form the total  $\chi^2$  of  $\chi^2 = \chi_{\text{CMB}}^2 + \chi_{\text{Hubble}}^2$ . We find  $w = -1.13 \pm 0.10$  and  $\Omega_m = 0.274 \pm 0.023$  (68% CL), in good agreement with the tSZ+ $H_0$  results. This shows that the tSZ power spectrum is a compelling probe for dark energy, complementary to distance-only constraints.

The predicted value of the matter fluctuation amplitude from the  $w$ CDM CMB+ $H_0$  is  $\sigma_8 = 0.844 \pm 0.030$  (68% CL). We obtained this by adding the information on the primordial power spectrum to our compressed likelihood (see last two rows of table 6). This is larger than what we find from the tSZ+ $H_0$  with  $B = 1.25$ . Had we chosen a larger mass bias, this apparent tension on  $\sigma_8$  would be alleviated, at the expense of making  $w$  more negative.

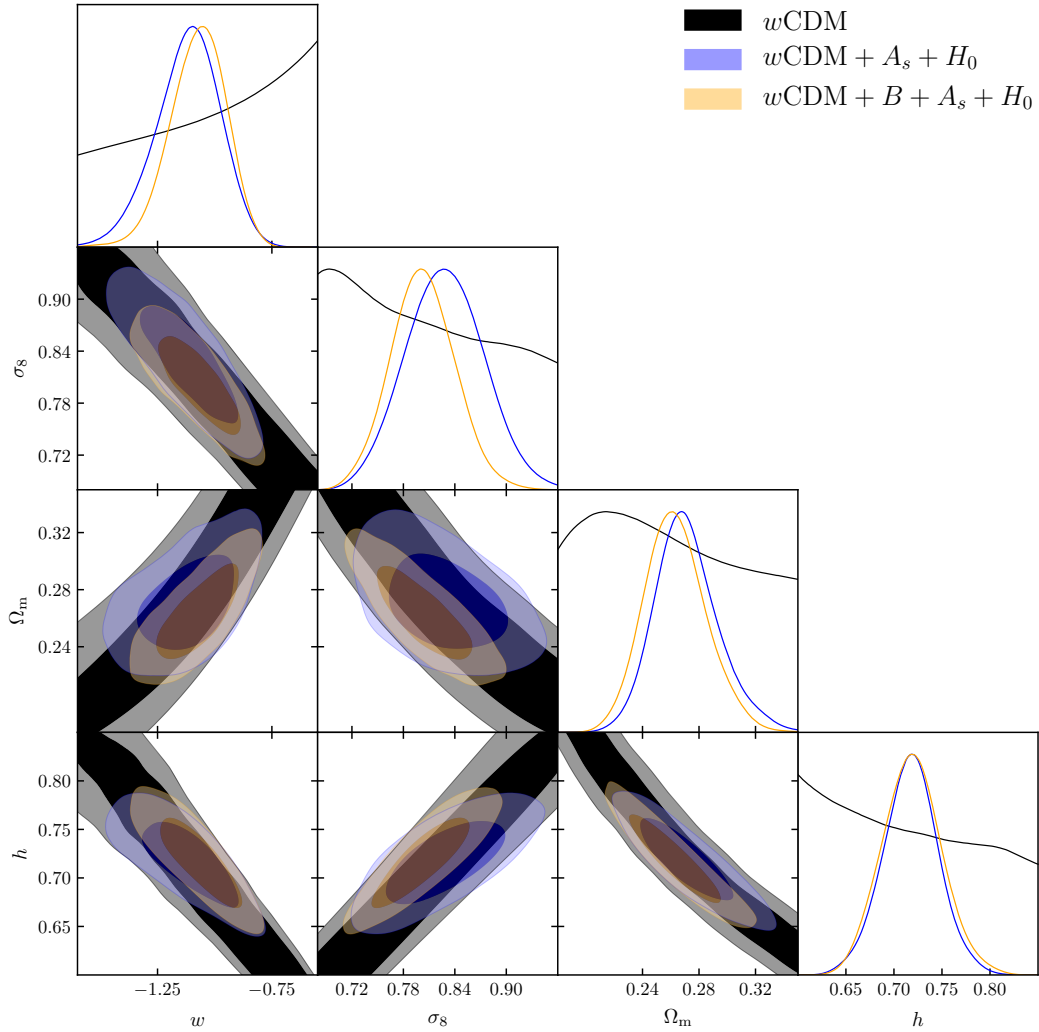


**Figure 6.** Marginalised (1D and 2D) joint posterior probability distributions of  $w$ ,  $\sigma_8$ ,  $\Omega_m$ , and  $h$ . The black contours show the constraints from the tSZ power spectrum alone, while the blue contours show those from the tSZ combined with a local measurement of the Hubble constant, the Planck amplitude prior (see table 5), and  $\tau_{\text{reio}} = 0.06 \pm 0.01$ , for a flat prior on the mass bias. We fix the mass bias to  $B = 1.25$  for the yellow contours.

	68% C.L.	$R$	$\ell_A$	$\Omega_b h^2$	$10^9 A_s$	$n_s$
$R$	$1.7447 \pm 0.0068$	1	0.51	-0.66	-0.58	-0.85
$\ell_A$	$301.70 \pm 0.14$	0.51	1	-0.44	-0.37	-0.45
$\Omega_b h^2$	$0.02228 \pm 0.00024$	-0.66	-0.44	1	0.39	0.61
$10^9 A_s$	$2.1108 \pm 0.0713$	-0.58	-0.37	0.39	1	0.60
$n_s$	$0.9681 \pm 0.0057$	-0.85	-0.45	0.61	0.60	1

**Table 6.** Posterior mean and covariance matrix derived from the Planck 2015 “lowTEB+lensing” chains of  $w$ CDM. The second column gives the the mean values and 68%CL standard deviations. The last five columns are the elements of cross-correlation coefficients  $D_{ij}$ .

## 6 SUMMARY AND CONCLUSIONS

In this paper we have improved upon the calculation and likelihood analysis of the tSZ power spectrum of resolved and unresolved galaxy clusters and groups in a number of ways, and derived a competitive constraint on the dark energy EoS parameter  $w$  from the amplitude of matter fluctuations.

First we identified the source of differences in the analyses based on the approach of Komatsu & Seljak (2002) and that of the Planck collaboration (Planck Collaboration 2013b, 2015): it is due to conversion of the virial mass to various over-density masses using some concentration-mass relations such as Duffy et al. (2008). Using HMF fits for  $M_{500c}$  eliminates sensitivity to the choice of concentration-mass relations.

For the first time we incorporated all the important elements of the likelihood analysis; namely, we include trispectrum in the tSZ power spectrum covariance matrix and vary the mass bias, the nuisance parameters, and all the relevant cosmological parameters in the MCMC exploration of parameters. The derived tSZ power spectrum with the nuisance parameters marginalised over is significantly lower than that derived from the Planck 2015 analysis (Planck Collaboration 2015), which did not include trispectrum, at  $\ell \gtrsim 300$ .

We find that the tSZ power spectrum amplitude at  $\ell \lesssim 10^3$  primarily depends on  $F = \sigma_8 (\Omega_m/B)^{0.40} h^{-0.21}$ . Using the tSZ power spectrum data alone we find  $F = 0.460 \pm 0.012$  (68% CL). In  $\Lambda$ CDM this implies a mass bias of  $B = 1.71 \pm 0.17$  or  $1 - b = B^{-1} = 0.58 \pm 0.06$  (68% CL) when combined with the Planck CMB data. This value agrees with that derived from the tSZ based cluster number counts (Planck Collaboration 2016b).

As dark energy slows down structure formation, we constrain  $w$  by combining the tSZ power spectrum, the primordial scalar amplitude constrained by the Planck CMB data, and local Hubble constant measurements. We find  $w = -1.15 \pm 0.15$  (68% CL) for  $1.11 < B < 1.67$  and  $w = -1.10 \pm 0.12$  (68% CL) for  $B = 1.25$ . These constraints are consistent with, and competitive and complementary to, more commonly studied distance-only constraints on  $w$  from CMB+ $H_0$ .

**ACKNOWLEDGMENTS**

We thank Ryu Makiya, Scott Kay, Jean-Baptiste Melin, Florian Ruppin, Fabien Lacasa, Guillaume Hurier, Jens Chluba, Laura Salvati and James Colin Hill for discussions as well as Thomas Tram and Julien Lesgourgues for their help with CLASS and Montepython. We thank Antony Lewis for suggestions regarding the contour plots made the GetDist software. We thank the referee for useful comments and suggestions that helped improving the presentation and interpretation of our results. This work was supported in part by JSPS KAKENHI Grants, JP15H05896 and ERC Consolidator Grant (CMBSPEC), No. 725456. This analysis is based on observations obtained with Planck (<http://www.esa.int/Planck>), an ESA science mission with instruments and contributions directly funded by ESA Member States, NASA, and Canada.

**REFERENCES**

Arnaud M., Pratt G. W., Piffaretti R., Böhringer H., Croston J. H., Pointecouteau E., 2010, *A&A*, **517**, A92  
 Audren B., Lesgourgues J., Benabed K., Prunet S., 2013, *JCAP*, **2**, 001  
 Bernal J. L., Verde L., Riess A. G., 2016, *JCAP*, **10**, 019  
 Blas D., Lesgourgues J., Tram T., 2011, *JCAP*, **7**, 034  
 Bocquet S., Saro A., Dolag K., Mohr J. J., 2016, *Mon. Not. Roy. Astron. Soc.*, **456**, 2361  
 Calabrese E., et al., 2017, *Phys. Rev.*, **D95**, 063525  
 Costanzi M., Villaescusa-Navarro F., Viel M., Xia J.-Q., Borgani S., Castorina E., Sefusatti E., 2013, *JCAP*, **1312**, 012  
 Dolag K., Komatsu E., Sunyaev R., 2016, *Mon. Not. Roy. Astron. Soc.*, **463**, 1797  
 Duffy A. R., Schaye J., Kay S. T., Dalla Vecchia C., 2008, *Mon. Not. Roy. Astron. Soc.*, **390**, L64

George E. M., et al., 2015, *Astrophys. J.*, **799**, 177  
 Hasselfield M., et al., 2013, *JCAP*, **7**, 008  
 Henson M. A., Barnes D. J., Kay S. T., McCarthy I. G., Schaye J., 2017, *Mon. Not. Roy. Astron. Soc.*, **465**, 3361  
 Horowitz B., Seljak U., 2017, *Mon. Not. Roy. Astron. Soc.*, **469**, 394  
 Hurier G., Lacasa F., 2017, *Astron. Astrophys.*, **604**, A71  
 Jenkins A., Frenk C. S., White S. D. M., Colberg J. M., Cole S., Evrard A. E., Couchman H. M. P., Yoshida N., 2001, *Mon. Not. Roy. Astron. Soc.*, **321**, 372  
 Klypin A. A., Trujillo-Gomez S., Primack J., 2011, *ApJ*, **740**, 102  
 Komatsu E., Kitayama T., 1999, *Astrophys. J.*, **526**, L1  
 Komatsu E., Seljak U., 2001, *Mon. Not. Roy. Astron. Soc.*, **327**, 1353  
 Komatsu E., Seljak U., 2002, *Mon. Not. Roy. Astron. Soc.*, **336**, 1256  
 Komatsu E., et al., 2009, *Astrophys. J. Suppl.*, **180**, 330  
 Komatsu E., et al., 2011, *Astrophys. J. Suppl.*, **192**, 18  
 Lau E. T., Kravtsov A. V., Nagai D., 2009, *Astrophys. J.*, **705**, 1129  
 Lesgourgues J., 2011, preprint, ([arXiv:1104.2932](https://arxiv.org/abs/1104.2932))  
 Lewis A., 2013, *Phys. Rev.*, **D87**, 103529  
 McCarthy I. G., Brun A. M. C. L., Schaye J., Holder G. P., 2014, *Mon. Not. Roy. Astron. Soc.*, **440**, 3645  
 Mukherjee P., Kunz M., Parkinson D., Wang Y., 2008, *Phys. Rev.*, **D78**, 083529  
 Penna-Lima M., Bartlett J. G., Rozo E., Melin J. B., Merten J., Evrard A. E., Postman M., Rykoff E., 2017, *Astron. Astrophys.*, **604**, A89  
 Planck Collaboration 2013a, *Astron. Astrophys.*, **550**, A131  
 Planck Collaboration 2013b, *Astron. Astrophys.*, **571**, A21  
 Planck Collaboration 2015, *Astron. Astrophys.*, **594**, A22  
 Planck Collaboration 2016a, *Astron. Astrophys.*, **594**, A13  
 Planck Collaboration 2016b, *Astron. Astrophys.*, **594**, A24  
 Salvati L., Douspis M., Aghanim N., 2017, preprint, ([arXiv:1708.00697](https://arxiv.org/abs/1708.00697))  
 Sánchez-Conde M. A., Prada F., 2014, *Mon. Not. Roy. Astron. Soc.*, **442**, 2271  
 Shi X., Komatsu E., 2014, *Mon. Not. Roy. Astron. Soc.*, **442**, 521  
 Shi X., Komatsu E., Nelson K., Nagai D., 2015, *Mon. Not. Roy. Astron. Soc.*, **448**, 1020  
 Sunyaev R. A., Zeldovich Y. B., 1972, *Comments on Astrophysics and Space Physics*, **4**, 173  
 Tinker J. L., Kravtsov A. V., Klypin A., Abazajian K., Warren M. S., Yepes G., Gottlöber S., Holz D. E., 2008, *Astrophys. J.*, **688**, 709  
 Tinker J. L., Robertson B. E., Kravtsov A. V., Klypin A., Warren M. S., Yepes G., Gottlöber S., 2010, *Astrophys. J.*, **724**, 878  
 Wang Y., Dai M., 2016, *Phys. Rev.*, **D94**, 083521  
 Weinberg D. H., Mortonson M. J., Eisenstein D. J., Hirata C., Riess A. G., Rozo E., 2013, *Phys. Rept.*, **530**, 87  
 Zhao D. H., Jing Y. P., Mo H. J., Boerner G., 2009, *Astrophys. J.*, **707**, 354